Behera and Sinha *EPJ Quantum Technology* (2024) 11:66
https://doi.org/10.1140/epjqt/s40507-024-00279-1

EPJ Quantum Technology
a SpringerOpen Journal

RESEARCH Open Access

Estimating the link budget of satellite-based Quantum Key Distribution (QKD) for uplink transmission through the atmosphere

Satya Ranjan Behera[1] and Urbasi Sinha[1*]

*Correspondence: usinha@rri.res.in
[1]Raman Research Institute, C.V. Raman Avenue, Sadashivanagar, Bengaluru, 560080, Karnataka, India

Abstract

Satellite-based quantum communications including quantum key distribution (QKD) represent one of the most promising approaches toward global-scale quantum communications. To determine the viability of transmitting quantum signals through the atmosphere, it is essential to conduct atmospheric simulations for both uplink and downlink quantum communications. In the case of the uplink scenario, the initial phase of the beam's propagation involves interaction with the atmosphere, making simulation particularly critical. To analyze the atmosphere over the Indian subcontinent, we begin by validating our approach by utilizing atmospheric data obtained from the experiments carried out in the Canary Islands within the framework of Quantum Communication (QC). We also verify our simulation methodology by reproducing simulation outcomes from diverse Canadian locations, taking into account both uplink and downlink scenarios in Low Earth Orbit (LEO). In this manuscript, we explore the practicality of utilizing three different ground station locations in India for uplink-based QC, while also considering beacon signals for both uplink and downlink scenarios. The atmospheric conditions of various geographical regions in India are simulated, and a dedicated link budget analysis is performed for each location, specifically focusing on three renowned observatories: IAO Hanle, Aries Nainital, and Mount Abu. The analysis involves computing the overall losses of the signal and beacon beams. The findings indicate that the IAO Hanle site is a more suitable choice for uplink-based QC when compared to the other two sites.

Keywords: Satellite QKD; Atmosphere; Link budget

1 Introduction

Towards the late 1980s, Bennett, Brassard, and their colleagues developed an experimental prototype in the IBM lab, enabling the successful implementation of a quantum key exchange. This was the first instance of free space QC being used for key exchange with the transmission distance limited to 320 mm [1–3]. Between 1990 and 2000, more free space QC has been conducted, with a 1-kilometer maximum distance [4–7]. In 2002, the National University of Singapore and the University of Vienna conducted free-space experiments, resulting in the successful distribution of entanglement over a distance of 7.8

kilometers during night-time [8]. When the distance between two locations is limited to a few kilometers [9–11], the impact of the atmosphere on QC is minimal. However, as the distance extends to tens of kilometers, the atmosphere becomes increasingly influential in QC. Yet, these studies do not offer detailed analyses of the contribution of the atmosphere to the signal. A noteworthy milestone was reached in 2007 with the collaboration of the European Space Agency (ESA) and SECOQC, where a significant quantum communication link spanning 144 km between the Canary Islands of La Palma and Tenerife was successfully established [12–14]. Due to the 144 km line of sight distance, the atmosphere played a significant role in this experiment. The communication channel involved in this study is horizontal. This experiment was conducted in actual atmospheric conditions, featuring channel attenuation similar to that encountered in an optical link between the ground and a low Earth orbit satellite. Therefore, it certainly demonstrates the viability of a technologically comparatively straightforward method for satellite-based quantum key distribution.

Fiber-based communication experiences considerable loss when the transmission distance is beyond the line of sight. To overcome this limitation, satellite-based techniques can be executed through uplink or downlink setups. In 2016, China successfully launched the world's first quantum communication satellite, marking a significant milestone in global quantum communication efforts [15–18]. This was a downlink communication system. In a downlink setup, communication involves a transmitter situated on the satellite and a ground-based receiver. This arrangement offers advantages like a high key generation rate due to reduced photon loss and minimal dark counts. Furthermore, it remains notably resistant to atmospheric turbulence. However, it's worth noting that placing the transmitter on the satellite contributes to an increase in the overall payload weight, potentially leading to escalated project complexity and costs.

On the contrary, the uplink configuration lacks constraints regarding photon source quantity or weight. It adds more flexibility to any change of the photon source required in the future, which is possible with the source on the ground. Also, it will allow for the inclusion of supplementary optical components, such as those required for error correction and characterization. However, in the case of uplink, the beam encounters the atmosphere in the initial stage of its propagation. The effect of the atmosphere on attenuating the link and reducing the key rate is unavoidable. Hence, atmospheric simulation plays an important role in modelling uplink compared to downlink-based QC.

In the realm of free-space quantum communication, a thorough grasp of atmospheric influences is required. These effects encompass phenomena like beam wandering, beam diffusion, scintillation, pointing error, and link attenuation as the transmitted beam navigates through a turbulent medium. This comprehension stands as a prerequisite for achieving effective communication between the satellite and the ground station. Various strengths of turbulence and their effect on quantum signals have been explained in [19]. A comprehensive numerical simulation was conducted, utilizing realistic simulated orbits and accounting for factors such as pointing error, diffraction, atmospheric conditions, and telescope design [20] for several geographic locations in Canada. This simulation aimed to provide estimates of the losses that a satellite-based system would encounter.

The Canary Island experiments [12–14] present experimental results, indicating complete losses where turbulence accounts for 18 dB, atmospheric transmittance contributes 15 dB, and the remaining losses are attributed to optical factors, resulting in a total loss

of 40 dB. The initial step involves simulating these outcomes with all the parameters to validate the loss values. The procedure's specifics are outlined in Sects. 5 and A.1 of the appendix. This horizontal free-space communication spanning 144 kilometers exhibits losses that are equivalent to those experienced in the LEO. In fact, simulations indicate that the anticipated link transmittance from an LEO satellite will be quite similar [21]. In contrast, the Canadian study [20], contains simulation findings of satellite loss in LEO orbit at various locations across Canada. To demonstrate that our simulation is accurate, we extended it to the LEO orbit and compared the findings with those from Canada. The detailed verification is given in A.2 of the Appendix. After comparing our simulation strategy with experimental results [12–14] and simulations conducted in other geographical regions [20], we proceed to apply it in detail to diverse scenarios within India. Specifically, our focus is on three distinct regions.

for three well-known observatories in the near-IR and optical bands. One of the observatories is the Indian Astronomical Observatory (IAO) in Hanle which is the highest astronomical observatory in India at 4500 meters altitude in the Himalayan region [22]. Situated in the Shivalik mountain range, the Aryabhatta Research Institute of Observational Sciences (ARIES) in Nainital serves as the second observatory [23]. ARIES is 1951 meters above sea level, and during the observation, the monsoon plays a crucial role. The third observatory is near Mount- Abu, which is located close to the Thar Desert at 1680 meters above sea level, where there is almost no rain for most of the year. The varied atmospheric conditions make India a fascinating study for varied geographical regions and their applicability to space-based QKD.

The manuscript is organized as follows: In Sect. 2, the loss budget between the satellite receiver and the ground station is calculated, whereas the same calculation is done for the beacon signal in Sect. 3. The key rate of two separate sources, i.e., weak coherent pulses (WCP) and entangled sources, is computed in Sect. 4 of the manuscript. Section 5 is the Conclusion section, and the final Section is the Appendix carrying additional information.

2 Link budget analysis

One of the first steps in building a line-of-sight communication system is creating a link budget, which serves many important purposes, including performance estimation before the link is formed, determining, often for a specified worst-case scenario, whether there is enough optical power to cross the link. Table 1 shows an example of the link budget calculation. For this, we have chosen IAO Hanle as the ground station location, and the satellite orbit at 500 km above the ground station at low earth orbit (LEO). The signal wavelength we have considered is 810 nm. The details of the parameters used for the link budget are discussed later in this section.

If P_t is the transmitted power then the detector aboard the satellite receives power P_r, which is given by [24].

$$P_r = P_0 IS\,, \tag{1}$$

P_0 is the received power in the absence of a turbulent atmosphere. It is assumed that the highest obtainable power is P_0, at the satellite. The next two parameters I and S are due to the atmosphere. I has a beta distribution due to atmosphere and pointing-related jitter, while S normally has a lognormal distribution as a result of scintillation [25].

Table 1 Link budget calculation for the IAO Hanle observatory. Rows 1, 2, and 3 represent parameters for the transmitter telescope. Rows 4 and 5 represent propagation loss. Rows 7, 8, and 9 represent parameters for the receiver telescope

No	Parameter	Unit	Signal
1	Tx gain (G_t)	dB	103.5
2	Tx Beam divergence ($2\Theta_B$)	μrad	19.85
3	Tx optics loss (η_t)	dB	–2.20
4	Path loss (L_r)	dB	–258
5	Atmospheric attenuation (η_{atm})=0.325	dB	–4.87
7	RX gain (G_r)	dB	121.35
8	RX optics loss (η_r)	dB	–2.2
9	RX pointing loss	μrad	2
10	Total loss	dB	44.26

In the absence of air turbulence, the received power at the satellite's detector is primarily affected by free-space propagation loss and optical absorption. When accounting for optical losses at both the transmitter and receiver, as well as atmospheric absorption, the resultant received power can be calculated as follows [26]

$$P_0 = P_t \eta_{atm}^{\sec\theta} L_r \eta_t \eta_r G_t G_r \,, \tag{2}$$

where G_t, which is the gain of the transmitter, G_r is the receiver telescope gain and L_r is the Free space propagation loss given by,

$$G_t = \frac{8}{\Theta_B^2}\,,\ G_r = \frac{4\pi A_r}{\lambda^2} \text{ and } L_r = \left(\frac{\lambda}{4\pi L}\right)^2. \tag{3}$$

Θ_B is the divergence of the laser beam in radians and L is the communication range in meters.

- η_t is the optical efficiency of the transmitter.
- η_r is the optical efficiency of the receiver.
- A_r represents the aperture area of the receiver, expressed in square meters.
- $\eta_{atm}^{\sec\theta}$ is the atmospheric attenuation at zenith.

Table 1 gives the link budget calculation.

The link budget for an optical system can be categorized into three main components: (i) Transmitter gains, which typically involve telescopes, and (ii) losses in optical path propagation. It's in two parts, losses through vacuum space and through the atmosphere, and finally (iii) the losses experienced by the received signal as it travels through the optical receiving components to reach the detector [27].

2.1 Transmitter

A telescope converts the source's quantum beam into a signal that is sent to the receiving satellite. The beam mainly depends upon the aperture size of the telescope and divergence. A smaller beam size leads to greater losses at the receiver due to its higher divergence. On the other hand, while a larger beam size exhibits less divergence, it becomes more susceptible to turbulence. Therefore, achieving an optimal beam size is crucial for improved performance. The gain of the transmitter beam [26], G_t is given in (3).

Θ_B is related to wavelength λ and beam size W_0 as $\Theta_B = \frac{\lambda}{\pi W_0}$.

The telescopes used are of Cassegrain-type architecture and the beams used are Gaussian type for both the transmitter and receiver side. Due to the obstruction of the secondary mirror, the overall transmittance of the telescope is given by [28]

$$\eta_t = \frac{2}{\alpha^2}\left(e^{-\alpha^2} - e^{-\alpha^2\gamma^2}\right)^2 \tag{4}$$

where $\gamma = \frac{b}{R}$. b is the secondary radius and R is the primary radius of the telescope.

$\alpha = \frac{R}{\omega}$. This ratio corresponds to the maximum fractional transmission by the telescope aperture. ω is the beam radius at the transmitter end.

2.2 Path loss

Here, the total path loss is categorized into two parts: one due to the satellite's distance from the Earth's surface, known as free space path loss, and the other arising from atmospheric conditions. The Earth's orbits are categorized into three distinct groups based on their altitudes, each serving specific purposes. The Geostationary Orbit (GEO) resides farthest from the Earth's surface, situated at an altitude of approximately 36,000 kilometers. In contrast, the Low Earth Orbit (LEO) is in the closest proximity to Earth, ranging from 200 to 2,000 kilometers in altitude, and it boasts the highest relative speed among these orbital categories. The Medium Earth Orbit falls between these two extremes [29].

Given its proximity to Earth, LEO experiences minimal diffraction loss, making it particularly advantageous for quantum key distribution (QKD) experiments. However, orbits with slower speeds, such as the Middle Earth Orbit (MEO) or GEO, offer the benefit of maintaining a continuous link for extended periods, allowing for prolonged QKD operations. Nonetheless, it's worth noting that MEO and GEO orbits come with their own challenges, including higher radiation levels and increased propagation loss.

Free space propagation loss [30] in dB is $\log_{10} L_r$ where L_r is given in (3).

2.2.1 Atmospheric loss

The atmosphere plays a crucial role in the quantum beam. The cause of atmospheric losses on the quantum beam can be divided into two parts. Such as static components and dynamic components. It can be written as

$$\eta_{atm} = \eta_{atte}\eta_{tur}\,, \tag{5}$$

η_{atte} is due to the static components of the atmosphere and η_{tur} is due to the turbulence i.e dynamic components.

The Static components constitute various types of gases, water vapors, and dust particles that constitute the static atmosphere. These atmospheric elements absorb energy from the photons and this phenomenon is known as absorption. It depends on the wavelength. Photon collisions with air particles cause scattering [31]. The dynamic components are discussed in the next 2.2.2 subsection.

Considering a collimated beam of initial beam intensity $I(0)$, after a path of length L, the atmospheric transmittance η_{atte} related to atmospheric attenuation may be described by

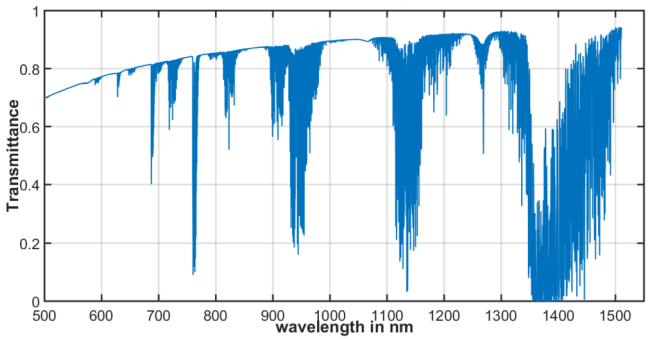

Figure 1 Simulated atmospheric transmittance at the IAO Hanle, a rural location. The X-axis represents the wavelength in nm, ranging from 500 to 1500, while the Y-axis represents the transmittance

Table 2 Atmospheric parameters considered for MODTRAN simulations for IAO Hanle

Atmospheric parameter	IAO
H_2O (g/cm3)	0.0865
CO_2 (ppm)	390
O_3 (g/cm3)	265
Aerosol RH	20
Visibility(km)	23
Rain (Mm/hr)	0.128
Climate	Mid-latitude winter
Model	Rural
Temperature (kelvin)	282
Altitude (meter)	4488
Reflectance	0.3

Beer's law as [32]

$$\eta_{atte} = \frac{I(L)}{I(0)} = e^{-\beta_{ext}(h,\lambda)L}, \tag{6}$$

where β is the extinction coefficient and h is the altitude.

A number of atmospheric radiative transfer software simulation packages have been developed to describe the effects of atmospheric absorption and scattering under different atmospheric conditions and over a large wavelength range. A popular computer program called MODTRAN models the atmosphere in the range of 100,000 nm (Far-IR) to 200 nm (UV). MODTRAN 6, is being employed in our simulation and offers a spectral resolution of $0.2cm^{-1}$ [33]. The transmittance of IAO Hanle is found and given in Fig. 1 The value of the atmospheric constituents is taken from GIOVANNI open source for the year 2015 from Jan to Dec. Giovanni stands for GES-DISC Interactive Online Visualization and Analysis Infrastructure. It is a web interface provided by NASA that allows users to explore gridded data obtained from various satellite and surface measurements [34]. Table 2 displays the parameters relevant to the MODTRAN plot.

Some commercially available laser systems such as those operating at 532 nm, 780 nm, 810 nm, 1060 nm, and 1550 nm, etc. have distinct transmission windows within this spectrum, where optical transmission encounters minimal loss. In general, higher wavelengths tend to offer improved transmission, but it's essential to consider other factors such as diffraction, as well as the capabilities of sources and detectors when determining the most

suitable wavelength choice. We use 810 nm as the main quantum signal beam and 532 nm and 1550 nm as the beacon beam for uplink and downlink respectively.

2.2.2 Turbulence

The structure constant C_n^2 is a common indicator of wave propagation over random media such as the atmosphere. It quantifies the variation in refractive index, denoted by n, caused by irregularities within the medium. To model the atmosphere effectively, it is essential to comprehend the altitude-dependent characteristics of the structure constant and its sensitivity to weather conditions. Accurately modeling the atmosphere poses a challenge, and different empirical and parametric theories have been developed to describe the altitude-dependent variations in the structure constant. There are various types of atmospheric models used, such as the Hufnagel-Valley (H-V) model, Polynomial Regression (PR) model, and Submarine Laser Communication (SLC) model etc. Out of these, the H-V model is widely utilized and is given by [35]

$$C_n^2(h) = 0.00594\left(\frac{v}{27}\right)^2 (10^{-5}h)e^{-10^{-3}h} + 2.7 \times 10^{-16} e^{-\frac{2h}{3\times 10^3}} + A_0\, e^{-10^{-2}h}. \tag{7}$$

Here h represents the altitude in meters relative to the specified location and the user is required to set the values of the parameters v and A_0 as indicated below.

The ground level turbulence strength is represented by A_0 in units of $m^{-2/3}$, while the root mean square (rms) wind speed at high altitude is denoted as v in meters per second. The H-V model provides a convenient way to adjust the profile of C_n^2 by modifying the values of the parameters A_0 and v. Standard value, for $A_0 = 1.7 \times 10^{-14} m^{-2/3}$ and $v = 21$ m/s [36].

An essential parameter for defining the turbulence and the nature of the wavefront propagating in the atmosphere is the atmospheric coherence length.

$$r_0 = 0.42k^2 \sec\theta \int_{h_0}^{Z} C_n^2(h)\, dh, \tag{8}$$

When there is no turbulence present, the parameter r_0 represents the diameter of an equivalent aperture where the resolution of a telescope is approximately diffraction-limited. A larger value of r_0 implies that turbulence has a lesser impact on the propagation of the beam and vice versa. Since r_0 varies with the wavelength according to $\lambda^{6/5}$, longer operating wavelengths result in larger values of the r_0. This suggests that at longer wavelengths, the effect of turbulence on the wavefront is less severe.

One more way to express the strength of turbulence is $\frac{D}{r_0}$. This is a ratio of the diameter of the beam from the telescope aperture to the atmosphere's coherence length. The higher the value, the more turbulated the beam. As the value for $\frac{D}{r_0}$ increases higher order wavefront distortion will accumulate [37]. Hence objective is to have minimum $\frac{D}{r_0}$. But its value shouldn't be < 1. Though no wavefront distortion will be there but optical beam will go through a beam wander phenomenon which makes it difficult to detect the beam at the receiver.

2.2.3 Beam divergence

Consider symmetric Gaussian beam propagation. In the absence of atmospheric turbulence, the intensity profile of the optical wave at the receiver in free space is given by: [38]

$$I_0(r,L) = \frac{W_0}{W^2} exp(-\frac{2r^2}{W^2}), \tag{9}$$

Here, W_0 represents the initial beam radius at the starting point where $L = 0$, L is the distance between the transmitter and the receiver. The W denotes the diffractive beam radius at the receiver, while r represents a vector perpendicular to the optical beam axis.

The average intensity of the optical wave received at the receiver under the influence of turbulence is given by

$$\langle I(r,L)\rangle = \frac{W_0}{W_e^2} \exp\left(-\frac{2r^2}{W_e^2}\right), \tag{10}$$

where W_e is the effective spot size of the Gaussian beam when atmospheric turbulence is present.

In order to measure the extent of beam spreading, the average effective beam waist is used to describe it as [26]

$$W_e^2 = W^2(1+T), \tag{11}$$

The parameter T characterizes the additional beam spreading caused by turbulence, which is dependent on the horizontal, uplink, and downlink beam paths as well as the turbulence intensity.

An uplink with a slant route and an angle θ from the zenith, T can be expressed as follows:

$$T = 4.35\chi^{5/6}k^{7/6}L^{5/6}\sec^{11/6}\theta \int_{h_0}^{h_0+L} C_n^2(h)(1-\frac{h-h_0}{L})^{5/3}dh, \tag{12}$$

where k is wave number, h_0 is altitude of the observer, $\chi = \frac{2L}{kW^2}$ is amplitude change due to diffraction.

2.2.4 Beam motion and jitter

When there's no turbulence, we can express the received signal as $I(r,L)$. L represents the propagation distance. However, in the presence of turbulence, the average of the received signal becomes $\langle I(r,L)\rangle$. It follows a probability density function denoted as $p(I)$ and its beta distribution $p(I)$ is given by [24]

$$p(I) = \beta I^{(\beta-1)}, \tag{13}$$

for $0 \le I \le 1$, $\overline{I} = \frac{\beta}{\beta+1}$ where I is the normalized intensity, $\overline{I}$ is the average value, and

$$\beta = \frac{\Theta_B^2}{4\sigma_j^2}, \tag{14}$$

The variance σ_j^2 is made up of the variance of atmospheric-induced and transmitter-induced pointing errors. The angle of arrival perturbation has a Gaussian distribution described by a zero mean and variance along the x and y axes as

$$\sigma_j^2 = 0.182 \left(\frac{D}{r_0}\right)^{\frac{5}{3}} \left(\frac{\lambda}{D}\right)^2, \tag{15}$$

Though more challenging to measure, the transmitter-induced jitter is often negligible in comparison to atmospheric effects. From Eq. (19). it can be concluded that either the beam jitter must be reduced or the angular beamwidth must be raised to attain a high value of β. In practice, one is frequently constrained to raising the beam divergence in order to get a certain value of β because one has little control over the atmospheric turbulence. However, the square of the beam divergence has an inverse relationship with the received power. Therefore, there is an optimum value of β that is dependent on the atmospheric conditions.

2.2.5 Atmospheric scintillation

The log-normal distribution for the Probability Density Function (PDF) of the normalized received intensity, denoted as S, is induced by scintillation. It is expressed as follows [39].

$$\sigma_l^2 = 2.24k^{7/6} \sec^{11/6}\theta \int_{h_0}^{L} C_n^2(h) h^{5/6} dh, \tag{16}$$

The variance of S itself is given by $\sigma_S^2 = \exp(\sigma_l^2) - 1$

2.3 Receiver

We considered having a 30 cm aperture size at the satellite receiver which is the maximum size allowed for a boarded satellite [40]. The transmittance is given by Eq. (2). The gain of the receiver telescope is given by [41]

$$G_r = \frac{4\pi A}{\lambda^2} \frac{2}{\alpha^2} \left[e^{-\alpha^2} - e^{-\alpha^2\gamma^2}\right]^2, \tag{17}$$

where $A = \pi \frac{D^2}{4}$ is the aperture area and D is the telescope diameter,

The pointing loss (l_p) is set at $2\mu rad$ at the receiver. The pointing loss is given by the formula [42]

$$l_p(\theta) = 4\left[\frac{J_1(p)}{p}\right]^2, \tag{18}$$

Where $p = \pi(\frac{D}{\lambda})\theta$

and λ is the wavelength, θ is the off-axis pointing angle, and J_1 is the Bessel function of order one.

Hence the complete equation for the received power in the presence of atmospheric turbulence is

$$P_r = P_t \eta_{atm}^{\sec\theta} L_r \eta_t \eta_r G_t G_r I S, \tag{19}$$

Table 3 Link budget for uplink 532 nm and downlink 1550 nm beam. Rows 1 to 6 represent parameter for the transmitter telescope. Rows 7 to 10 represent propagation losses. Rows 11 to 13 represent parameters for the receiver telescope

No	Parameter	unit	Uplink	Downlink
1	Tx power (P_t)	W	1.0	1.0
2	Tx Beam waist($1/e^2$)	mm	150.0	300.0
3	Wavelength (λ)	nm	532	1550
4	Tx Beam divergence ($2\Theta_B$)	μrad	500	500
5	Tx optics loss (η_t)	dB	–2.20	–2.20
6	Tx gain (G_t)	dB	71.23	69.06
7	Propagation distance (L)	km	500	500
8	Path loss (L_r)	dB	–258	–258
9	Atmospheric absorption (τ_{atm})=0.7/0.8	dB	–1.55	–0.97
10	Turbulence (τ_{tur})=0.5	dB	–3	–3
11	RX antenna diameter	cm	30.0	15.0
12	RX gain (G_r)	dB	125.0	118.65
13	RX optics loss (η_r)	dB	–2.2	–2.2
14	total loss	dB	72.36	74.56

Where I and S are random variables in the above equation. The PDF of the received signal can be represented by the product of the random variable I following a beta distribution and the random variable S following a lognormal distribution.

3 Link budget calculation for beacon beams

To establish and sustain a free-space optical link, it is essential for the spacecraft's altitude determination and control system to ensure precise pointing accuracy toward the optical ground station. Conversely, a laser beacon tracking system has the capability to furnish accurate ground-based altitude information, thus facilitating communication from the satellite. A laser beacon is transmitted from the optical ground station with a different wavelength from the quantum signal beam. The satellite will also transmit a beacon beam to get the position of the ground station. For the uplink, we use 532 nm, and for the downlink beacon 1550 nm wavelength. The link budget calculation for the beacon beam is also given in Table 3 for a ground telescope of 15 cm aperture and a satellite telescope of 30 cm aperture [43]. The calculation for the optimum size of 15 cm is given in Sect. A.4 of the Appendix.

To summarize the information contained in the various tables, the first Table 1 provides the link budget for the signal beam at the IAO Hanle observatory. The atmospheric parameters for the period from January to December 2015 which are sourced from the GIOVANNI database presented in Table 2. Table 3 presents the link budget for the uplink and downlink beacon beams at IAO Hanle. Finally, Table 4 compares the link budget analysis for the signal and beacon beams between IAO Hanle, Aries Nainital, and Mount Abu. For a comprehensive understanding of the parameters employed to compute the link budget for these two observatories, please refer to Table 11 within the Appendix section. The beacon beam at 532 nm is used for uplink and 1550 nm for downlink, whereas the last column for the signal beam is at 810 nm. For the downlink beacon due to the smaller size of the ground telescope, the loss is approximately 2 dB more compared to the uplink.

A conclusion can be made that IAO Hanle is more suitable for establishing a ground-to-satellite communication channel compared to the other two observatories due to less loss in both uplink and downlink for the signal as well as beacon beams.

Table 4 Link budget analysis for 3 different locations in India for uplink beacon, downlink beacon and signal beam of wavelength 532 nm, 1550 nm and 810 nm respectively

Location	Uplink beacon loss in dB	Downlink beacon loss in dB	Signal loss in dB
IAO Hanle	72.36	74.56	44.28
ARIES Nainital	74.17	76.48	48.8
Mount-Abu	75.85	78.16	47.50

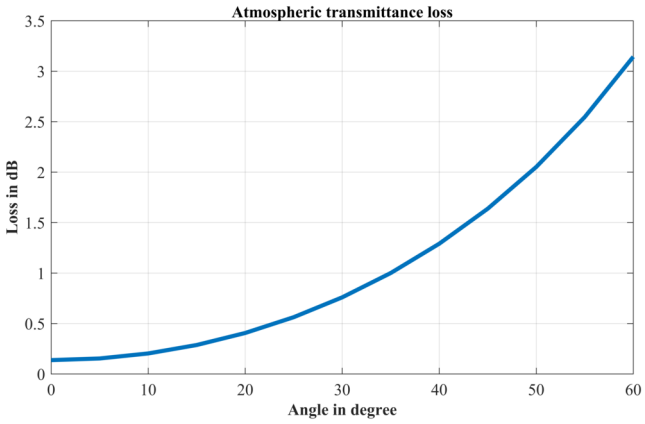

Figure 2 Atmospheric transmission at different zenith angles. X-axis represents the zenith angles in degree. Y-axis represents the loss in dB which will accumulate with increase in angle

When the zenith angle is zero degrees, the loss is indicated in Table 4 for the three separate places in India. The air mass will increase when the satellite moves at a greater zenith angle, which is the cause of an increase in loss in dB, as depicted in Fig. 2. The plot is given for one of the locations i.e. IAO Hanle.

The uplink signal loss will rise cumulatively as the satellite passes the vertical direction with increasing zenith angle. The overall cumulative loss is only 5 dB up to 45°. But at 60°, it doubles to 10 dB. Hence, the overall losses at a larger zenith angle are more i.e. the beam passes through the more turbulent region.

3.1 Doppler effect assessment

In the case of a LEO satellite, the apparent velocity relative to the ground exhibits a linear increase as the satellite's elevation angle rises. This scenario involves an analysis of the Doppler effect. As per the Doppler effect, the central frequency of the signal undergoes substantial changes during the data transmission and communication process, primarily due to the rapid motion of LEO satellites. If the satellite receiving end moves away from the transmitting ground end, the signal frequency will decrease, potentially resulting in a higher error rate upon signal reception and recovery. Normalized Doppler $\frac{\Delta f}{f}$ is given by [44]

$$\frac{\Delta f}{f} = \frac{-1}{c} \frac{r_E r \sin(\psi(t) - \psi(t_0)) \cos(\cos^{-1}(\frac{r_E}{r} \cos\theta_{max}) - \theta_{max}) \omega_f(t)}{\sqrt{r_E^2 + r^2 - 2 r_E r \sin(\psi(t) - \psi(t_0)) \cos(\cos^{-1}(\frac{r_E}{r} \cos\theta_{max}) - \theta_{max})}} \tag{20}$$

where,

- r_E= radius of earth which is 6400 km

- r = position of satellite w.r.t center of earth which is 6900 km
- $\psi(t) - \psi(t_0)$ is satellite visibility window duration which is 8 min. approx.
- θ_{max} is maximum elevation angle which is 90 degrees.
- $\omega_f(t)$ angular speed of satellite which is 0.00105 rad/sec
- c is the velocity of light.

For 810 nm signal beam the $\frac{\Delta f}{f}$ comes out to be 1.5×10^{-5}. Correspondingly the frequency shift Δf w.r.t the center carrier frequency 380 THz is 0.0057 THz. This shift is considered negligible.

4 Polarization-based quantum communication protocol simulations

Polarization is a fundamental property of photons given by the plane in which the electric field vector oscillates. Polarization states can be represented as vectors in a two-dimensional Hilbert space [45]. Different mutually unbiased bases in this degree of freedom, like {horizontal (H), vertical (V)}, {diagonal (D) and anti-diagonal (A)} and {right-circular (R) and left-circular (L)}, can be used to create bipartite polarization-entangled states. For example, an entangled pair can be represented as

$$\psi = \frac{1}{\sqrt{2}}(H_A V_B + V_A H_B) \tag{21}$$

where subscripts A and B denote two different photons.

Polarization states are used to encode information. To measure the polarization of a photon, polarizing beam splitters and waveplates are used. The measurement outcomes depend on the chosen basis (e.g., H/V basis or D/A basis). In the following Sect. 4.1, we discuss atmospheric effects on polarization, that can cause error in measurement results. Protocols like BB84 with weak coherent pulse sources use polarization states to generate and share cryptographic keys. Details are given in Sect. 4.2, whereas QKD using an Entangled source is discussed in Sect. 4.3.

4.1 Effect of atmosphere on polarization degree of freedom

In Free-Space QKD, one of the key challenges is the impact of atmospheric turbulence on the polarization state of photons used for encoding quantum information. As polarized photons propagate through the atmosphere, they are subject to turbulence, which can cause random fluctuations in the refractive index of the air causing an effect of birefringence (See the discussion in 2.2.2). These fluctuations affect the phase of orthogonal polarization components differently, leading to a change in overall polarization state of the photons. This leads to a higher Quantum Bit Error Rate (QBER), as the transmitted polarization state may not match the intended one. These effects of turbulence on polarization state and possible mitigation strategies are as follows:

Depolarization: Turbulence can mix different polarization components, converting pure polarized states into partially or completely depolarized mixed states. Such errors in the real world implementation can be countered using adaptive optics based solution that corrects for any wavefront distortion caused during transmission.

Birefringence: Variations in refractive index along different propagation axes create an effect of birefringence, causing phase shifts between different polarization components. There have been successful demonstration of various active [46, 47] and passive [48] polarization correction techniques that corrects for any polarization scrambling because of birefringence in free-space or in fiber based systems.

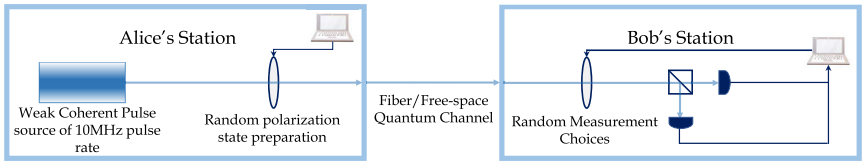

Figure 3 Block diagram of the BB84 QKD protocol using WCP source with source rate of 10 MHz

4.2 Simulated results from QKD utilizing a weak coherent pulse (WCP) source

QKD can be categorized into two primary types: Discrete Variable QKD (DV-QKD) and Continuous Variable QKD (CV-QKD). DV-QKD systems are further divided into prepare-and-measure protocols and entanglement-based protocols. In a typical prepare-and-measure protocol, Alice encodes each classical bit to a state of a quantum system and sends it to Bob, who performs a specific set of measurements on the incoming signals to retrieve the classical data encoded in their states. In the BB84 protocol, the most widely used prepare-and-measure QKD protocol, each classical bit is encoded into the polarization of a single photon. Alice randomly selects a basis between the horizontal/vertical (Z basis: H, V) and the +45°/-45° (X basis: A and D) and assigns bit values of 0 and 1 to these states. She then sends the chosen photon state to Bob. Bob randomly selects a basis to measure the incoming photon and records the result as a classical bit. After many transmissions, Alice and Bob publicly announce their chosen bases for each photon and discard cases where their bases do not match. They then estimate the error rate from a random subset of their data. If the error rate is low enough, below the security threshold, they apply error correction and privacy amplification to obtain a final shared secret key. A block diagram of BB84 using WCP is given in Fig. 3.

For our simulation, we have assumed a WCP source of 10 MHz pulse repetition rate with a mean photon number(μ) of 0.5. Considering this configuration for the source and equivalent sender and receiver optics and detection system, we have applied our link budget analysis to the potential ground station locations under consideration for quantum communication to an LEO satellite.

In the practical implementation of weak coherent pulses in QKD, the quantum link becomes prone towards eavesdropping strategies like photon number splitting attacks. Hence, decoy states are introduced in many experimental demonstrations to prevent potential Eaves from gaining any useful information during the communication [49].

In this work, we have assumed such a decoy state-based system and estimated key rate and QBER considering quantum links from various ground stations in India with fixed source parameters. The quantum bit error rate for a decoy-state protocol is represented as E_μ and given as [50],

$$E_\mu = \frac{\frac{Y_0}{2} + e_{detector}(1 - e^{(-\eta\mu)})}{Q_\mu} \tag{22}$$

where Y_0 is the dark count of the detector, Q_μ denotes the signal gain, η is the detection efficiency and $e_{detector}$ is the probability of erroneous detection.

Table 5 Estimated QBER and keyrate for 3 different locations in India considering WCP source based decoy state QKD protocol

Observatories	Loss (dB)	QBER for WCP in %	Keyrates for WCP in bps
IAO Hanle	44.28	4.25	2079
ARIES Nainital	48.81	8.81	857
Mount-Abu	47.50	7.41	1009

Following the same reference, the asymptotic key rate per pulse was calculated, which has a lower constraint using the decoy state approach, which is given by

$$K \geq q\frac{N_\mu}{N_\mu + N_v}\Big[- Q_\mu f(E_\mu)H_2(E_\mu) + Q_1\{1 - H_2(E_1) - \frac{Q_\mu \Delta}{N_\mu}\}\Big], \tag{23}$$

In this context, the parameters are defined as follows: $q = 1/2$ represents the basis reconciliation factor, $f(E_\mu) = 1.22$ stands for the error correction efficiency for practical error correction codes. The binary entropy function is denoted as $H_2(x)$. Finally, Q_1 and E_1 correspond to the estimated gain and error rate for single-photon pulses. where N_μ (N_v) is the number of Bob's received signal (decoy) counts. The security parameter Δ is given by

$$2\log_2 \frac{1}{[2(\epsilon - \overline{\epsilon} - \epsilon_{EC}) + 7\sqrt{N\log_2[\frac{2}{\overline{\epsilon}-\overline{\epsilon}^2}]}]}, \tag{24}$$

where N is the length of the raw key,

The QBER and key rate calculations for three different observatories are given in Table 5

It can be concluded that all three observatories have QBER less than the information-theoretic security threshold of 11% meant for BB84 protocol.

4.3 Results from QKD simulations using an entangled photon source

Entanglement-based protocols differ from prepare-and-measure systems by eliminating the need for active state encoding. In this work we consider BBM92 QKD protocol. Alice and Bob share a source of maximally entangled photon pairs. These photon pairs are entangled in polarization, with one photon belonging to Alice and the other to Bob. Both Alice and Bob independently choose to measure the photons on either a linear or diagonal polarization basis [51]. A block diagram of an Entangled source-based QKD protocol is given in Fig. 4.

The transmitter module includes an entangled photon source of 10 MHz pair generation rate. Both Alice and Bob, acting as receivers, have identical polarization-measuring optical setups, each followed by single-photon detectors. A block diagram of BBM92 using entangled photon source is given in Fig. 4

The asymptotic key rate per signal for the BBM92 QKD protocol is given by

$$K = \frac{1}{2}\Big[1 - H_2(E) - f(E)H_2(E) - \Delta/N\Big], \tag{25}$$

Here E is the QBER of the signal source. The total number of signals sent by Alice N. The term $f(E)H_2(E)$ is essentially equal to the measure of the key bits that are transmitted over the public communication channel for error correction purposes. The quantity Δ is the number of key bits required for error correction and privacy amplification. $H(x)$ is the

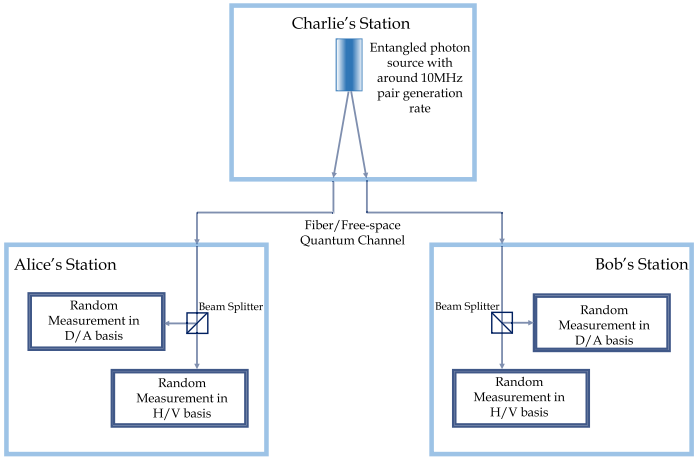

Figure 4 Blcok diagram of the BBM92 QKD protocol using entangled photon source with 10 MHz pair generation rate

Table 6 QBER and key rate calculation for 3 different locations in India for Entangled sources

Observatories	Loss (dB)	QBER for Entangled source in %	Keyrates for Entangled source in bps
IAO Hanle	44.28	5.26	1052
ARIES Nainital	48.81	9.82	99
Mount-Abu	47.50	8.42	107

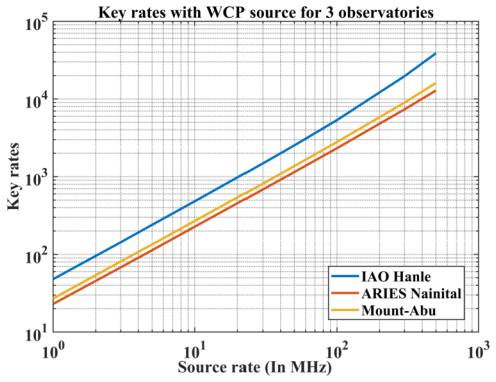

Figure 5 Key rate estimation with BB84 protocol considering WCP source for three different observatories

binary entropy function. All the parameters used in the equations have been taken from [52]. The QBER and key rates calculations for Entangled sources are given in Table 6 for the three observatories.

It can be concluded that all three observatories have QBER less than the information-theoretic security threshold of 11% meant for the BBM92 protocol.

Figure 5 and Fig. 6 display the final key rate for both Weak Coherent Pulse (WCP) and Entangled sources for all 3 observatories. The X-axis represents the source rate of the transmitter, while the Y-axis represents the final key rate. The graph includes four detectors, indicating the ratio of the detection window to the repetition period (1.0 ns to 10 ns), and Alice's detection efficiency of 0.25.

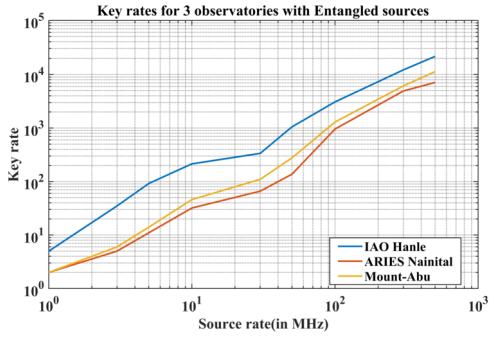

Figure 6 Key rate estimation considering an Entangled source-based QKD for the three potential observatory loactions

Table 7 Link budget analysis for 3 different potential locations as ground stations in India

Observatories	Loss (dB)	WCP (bits/sec)	Entangled (bits/sec)
IAO Hanle	44.28	2079.55	1052.11
ARIES Nainital	48.81	857.25	99.23
Mount-Abu	47.50	1009.16	107.56

By integrating quantum optics simulations for sources and detectors, we ascertain the length of secure keys for Quantum Key Distribution (QKD). This assessment includes considering uplink scenarios for both Weak Coherent Pulse (WCP) and entangled photon sources, each operating at a source rate of 10 MHz. Quantum Bit Error Ratios (QBERs) and sifted key rates are computed and serve as the basis for determining the extent of secure keys. This analysis encompasses all three observatories in the study and is given in Table 7.

From Table 7, it can be concluded that WCP sources have higher key rates compared to Entangled sources at all the three observatories. QBER for both types of sources for all three observatories is less than 11%. The schematic provided for the QKD experiments confirms these results.

5 Conclusion

We have presented simulation results analyzing the link performance at three different locations in India. The source being at the ground station, atmospheric effects become more prominent. Consequently, we compared atmospheric absorption using MODTRAN and calculated turbulence-related losses for all observatories. Our findings reveal that the Indian Astronomical Observatory (IAO) in Hanle exhibits the best performance, with total losses of approximately 44 dB. It's important to note that due to turbulence, the beam also experiences increased divergence. Therefore, we have opted for an optimal aperture size of 15 cm, as going smaller results in higher losses, while going larger leads to a more turbulent beam, which in turn reduces the Strehl ratio at the detector. To further enhance performance, additional technologies like Adaptive Optics will be employed.

Appendix: Quantum communication in Canary island

An experimental evaluation was conducted to assess the practicality of a satellite-based global quantum key distribution (QKD) system. The experiment involved a free-space

Table 8 Parameters used to calculate loss between La Palma and Tenerife island

Nordic Optical Telescope (NOT) transmitter	150 mm
NOT altitude	2381 m
Optical Ground Station (OGS) receiver	1 m
OGS altitude	2393 m
Link distance	143.6 km
Quantum wavelength	850 nm
Beacon wavelength	532 nm
C_n^2 value by H/V model	1.7×10^{-14}
Fried parameter r_0	5 cm (500 nm)

Table 9 Different types of losses for different wavelengths between the two considered islands

λ in nm	Θ_t in μ radian	W_{eff} in m	L_A in dB	L_T in dB	L_{ee} in dB
532	23.6	3.4	13.5	14.2	31.7
850	39.6	5.7	18.8	18.7	41.5

QKD setup over a real distance of 144 kilometers [14]. The Canary Islands of La Palma and Tenerife were selected as the testing locations, with both sites equipped with transmitter and receiver units positioned at an altitude of 2500 meters. The transmission of attenuated laser pulses from the compact and portable transmitter unit to the receiver was facilitated using a 15-cm optical telescope.

From [14], Table 8 gives the total specifications in detail for the two islands' communication.

End-to-end transmission losses L_{ee} were determined by comparing the intensity before the transmitter lens and after passing through the optics of the OGS telescope at the Coude focus. Comparable optical power meters were used for this comparison. These losses encompass four distinct processes, all contributing to L_{ee}.

The total transmission losses L_{ee} can be broken down into four components:

L_0: Beam spreading loss caused by diffraction, which exists even in a vacuum.

L_A: Atmospheric losses resulting from scattering and absorption by air molecules.

L_T: Turbulent atmospheric losses caused by beam spreading due to turbulence.

L_I: Losses due to imperfections in the optical components.

Additionally, the attenuation introduced by the transmitter and receiver telescope optics up to the Coude focus accounted for an approximate attenuation of 4 dB.

The following Table 9 presents the measured parameters during a specific nighttime observation. The absorption- and scattering-induced losses, denoted as L_A, for light at wavelengths 532 nm and 850 nm appear to range between 6 dB and 18 dB and 10 dB and 19 dB, respectively.

A.1 Validation of losses observed in Canary island

The atmospheric mode chosen is the standard Hufnagel-valley model (H/V) with $A = 1.7 \times 10^{-14}$ and the Fried parameter is chosen 5 cm for 500 nm. The L_T matches with the table given for a transmitter beam radius of 15 cm for a distance of 144 km in horizontal propagation. For horizontal links, one can use a semiempirical method to describe and scale the scattering extinction coefficient. For a wavelength of $\lambda = 550nm$, the visual range V is defined as the distance in (Km) in a horizontal path with constant scattering. On a normal clear day, the visual range can have a value of V of up to 23 kilometers, but on a cloudy day, it can only be as low as 5 kilometers.

Table 10 Parameters used in MODTRAN simulations for Canary islands

Model	Mid-latitude
Relative Humidity (RH)	90 %
Aerosol model	Maritime
Visibility	5 km
Optical depth	3.778
Altitudes	2400 meter

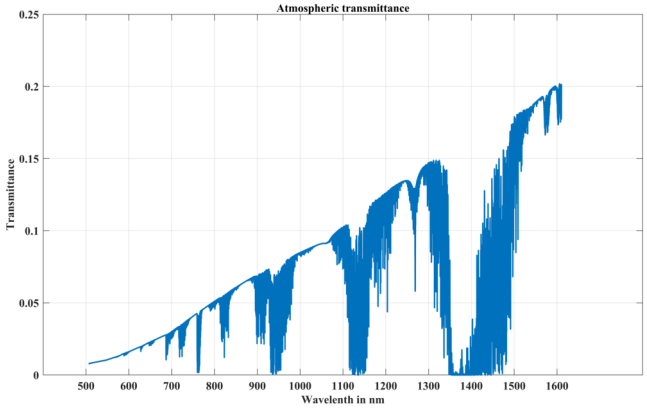

Figure 7 Atmospheric transmittance of Canary islands. X-axis represents wavelength in nm from 500 to 1500. Y-axis represents the transmittance value

The MODTRAN plots the transmittance with respect to the wavelength. For horizontal transmission T_h over a path (L) at any altitude (h), the attenuation Coefficient T_h [53].

$$T_h = e^{-\beta_{ext}(h,\lambda)L}. \tag{A.1}$$

This expression is known as Beer-Lambert law which is the ratio of the collimated beam after propagating distance L, $I(L)$ with initial beam intensity $I(0)$ then $\frac{I(L)}{I(0)} = T_h$

The MODTRAN parameter is given in Table 10 for the plot of atmospheric transmittance with the wavelength for the Canary Island [14] is given in Fig. 7. From this plot, it can be concluded that the transmittance at 850 nm matches the loss given in Table 9.

A.2 Verification of Canadian data through simulation

The Canadian Quantum Encryption and Science Satellite mission at the University of Waterloo proposed the uplink as well as downlink QKD experiment for the Ottawa location in Canada for an LEO orbit satellite. This location is situated in the sub-Arctic region with an altitude of 70 m, and a sea-level rural atmosphere with a visibility of 5 km [13]. The plot is given in Fig. 8.

A.3 Modtran parameters for three Indian observatories

Table 11 gives the Modtran parameter used for three Indian observatories. Figure 9 gives a comparison atmospheric transmittance plot for these three observatories.

A.4 Telescope size optimization

The atmosphere plays a major role when a beam in the optical domain propagates through it. Turbulence degrades its quality. The turbulence strength can be measured with Fried

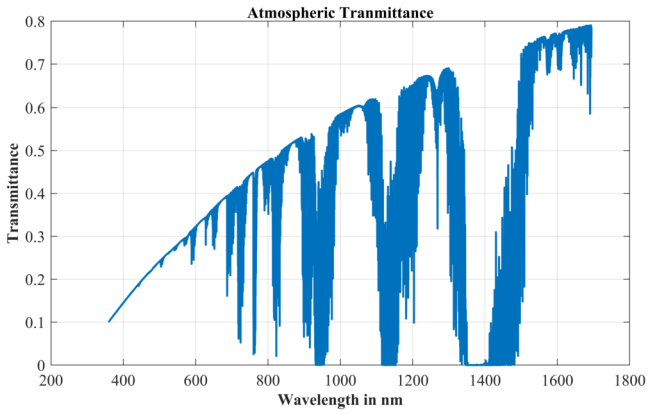

Figure 8 Atmospheric transmittance from the considered Canadian location(Ottawa)

Table 11 Atmospheric parameters considered in MODTRAN simulations for IAO Hanle, Aries Nainital and Mount-Abu

Atmospheric parameter	IAO	Aries	Mount-Abu
H_2O (g/cm3)	0.0865	0.2489	0.1732
CO_2 (ppm)	390	322	364
O_3 (g/cm3)	265	277	270
Aerosol RH	20	50	65
Visibility(km)	23	23	23
Rain (Mm/hr)	0.128	1.29	0.82
Climate	Mid-latitude winter	Tropical	tropical
Model	Rural	Rural dense	Rural
Temperature (kelvin)	282	292	290
Altitude (meter)	4488	1895	1220
Reflectance	0.3	0.177	0.204

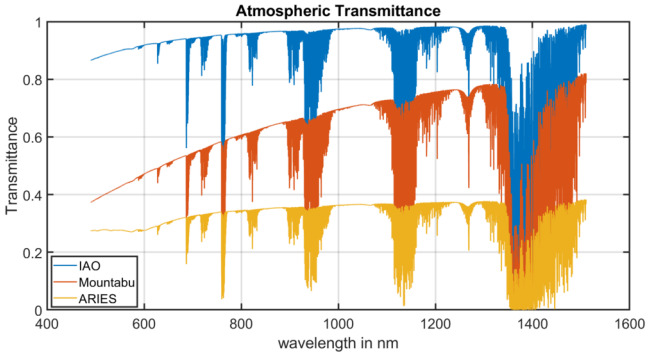

Figure 9 Atmospheric transmittance comparison of three potential observatory locations

parameter r_0. The main objective is to have a bigger value of the Fried parameter. If D= diameter of the beam from the telescope then a quantity $\frac{D}{r_0}$ is a ratio of the diameter of the beam from the telescope to the diameter of the turbulence strength i.e. Fried parameter. The lesser the value is better. Ideally, the value is ≤ 1. For $(\frac{D}{r_0}) > 1$ indicates that the beam is more turbulent at the focal point, leading to a degradation in beam quality. As this value increases, it results in greater losses at the detector, as illustrated in the Fig. 10. However,

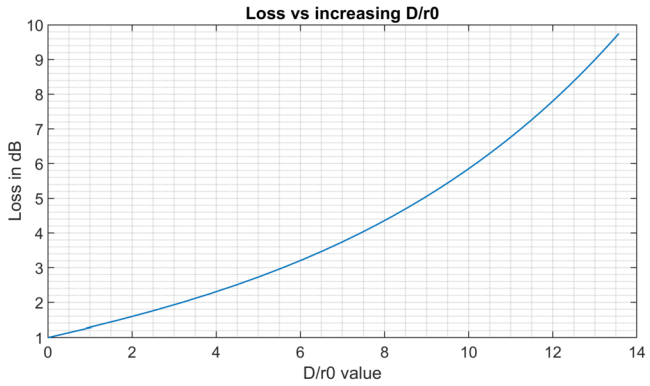

Figure 10 The plot of increasing $\frac{D}{r_0}$ value vs loss in dB

after $(\frac{D}{r_0}) > 2$ the degradation of beam starts rapidly [26]. It can be concluded that $(\frac{D}{r_0})$ in between 1 to 2 is safe to operate.

Turbulence and optical aberrations can cause a reduction in the intensity of the beam detected by the satellite. This change is quantified by the Strehl ratio (S), which represents the ratio of the measured on-axis intensity of the detected spot to the intensity of a spot that would be diffraction-limited.

$$\langle S \rangle = \frac{\langle I(L) \rangle}{\langle I(0) \rangle} = \left[1 + \left(\frac{D}{r_0} \right)^{5/3} \right]^{-6/5}, \quad 1 < \frac{D}{r_0} < \infty \tag{A.2}$$

Which implies that S decreases with increasing $(\frac{D}{r_0})$ causing difficult to detect at the detector [54].

When the ratio $(\frac{D}{r_0})$ is less than 1, it leads to the phenomenon of beam wander, which results in instability in the beam. This instability makes it challenging to precisely align the beam with the detector, leading to an increase in pointing errors. Beam wander is given by [55]

$$\langle r_c^2 \rangle = 0.73 Z \sec \zeta \left(\frac{\lambda}{2W_0} \right) \left(\frac{2W_0}{r_0} \right)^{5/6} \tag{A.3}$$

Where $\langle r_c^2 \rangle$ is variance of beam shifting and $sec(\zeta)$ is the elevation angle of the beam from the ground station.

A.4.1 Beam divergence under turbulence

Optical beams through the atmosphere can be studied by Andrews and Philip's proposed PDF (probability density function) known as I-K distribution. This PDF is expressed in terms of Bessel functions and can be used to characterize turbulent optical channels over a wide range of operating conditions. Optical field intensity at the receiver is given by

$$\langle I(x, y, t) \rangle = \frac{P_t G_a}{4\pi Z^2} \eta_t \eta_r \eta_{atm} I_u \exp\left(-\frac{4(x^2 + y^2)}{\Phi_B^2 Z^2} \right) \tag{A.4}$$

- $\eta_{t,r,atm}$ represents the transmittance of the transmitter, receiver telescopes, and atmosphere respectively.

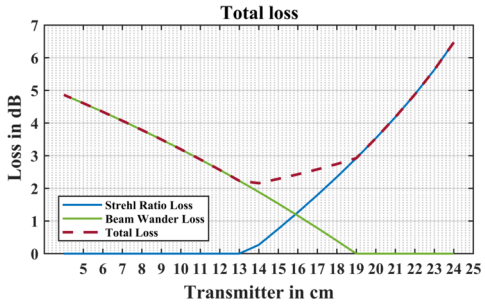

Figure 11 Beam wander and Strehl ratio losses for different initial beam sizes

Table 12 Final loss for different initial beam sizes

D in cm	8 cm	12 cm	14 cm	15 cm	16 cm	20 cm	24 cm
Loss in dB	47.47	46.57	46.33	46.22	46.12	46.04	45.7
Beam wander loss	3.53	1.27	0.27	0.12	0	0	0
Strehl ratio loss	0	1.17	1.89	2.20	2.56	3.79	4.86
Final loss in dB	51.0	49.0	48.49	48.52	48.68	49.83	50.56

- p_t is the transmitted power.
- Z is the propagation distance.
- Θ_B is the beam divergence angle.
- I_u is the random variable due to atmosphere scattering.

The PDF of I_u follows β distribution. Where $\beta = \frac{\Theta_B^2}{4\sigma_{jit}^2}$

σ_{jit}^2 1-axis 1- jitter variance which can be represented by

$$\sigma_{jit}^2 = 0.36 \left(\frac{D}{r_0}\right)^{5/3} \left(\frac{\lambda}{D}\right)^2 \tag{A.5}$$

Either the angular beam width or the beam jitter must be decreased in order to attain a high value of β. In practical scenarios, it is often necessary to increase the beam divergence to achieve a desired value of β due to the limited control over atmospheric turbulence-induced beam wander. However, the square of the beam divergence has an inverse relationship with the received power. Therefore, there is an ideal value of β that is dependent on the atmosphere.

A smaller beam diameter will primarily experience beam wander losses, while a larger beam diameter will primarily incur Strehl ratio losses. These losses contribute to the overall total loss. Therefore, the optimal beam size is one that minimizes the combined impact of these two losses, resulting in the lowest total losses.

From Fig. 11. it can be concluded that the beam size 14-15 cm has the minimum losses. Table 12 gives the final loss calculated for IAO Hanle for different beam sizes.

Acknowledgements
We acknowledge Animesh Sinha Roy for his technical assistance with the quantum signal and final key rate analysis. SRB thanks Saumya Ranjan Behera, Melvee George, and Mehak Layal for proofreading the manuscript. Lastly, we thank Kallon Sen for his technical assistance.

Author contributions
SRB performed the analysis under US's supervision. Both authors contributed to the writing of the manuscript.

Funding
The work has been provided by the Indian Space Research Organization (ISRO) through the QUEST (Quantum Experiments using Satellite Technology) research grant.

Data Availability
No datasets were generated or analysed during the current study.

Declarations

Ethics approval and consent to participate
The authors US and SRB have followed the research ethics guidelines during the entire course of the work. The work has been completed with the full consent to participation from both the contributing authors.

Consent for publication
All the contributing authors (US and SRB) consent to the publication of this work in the journal. Both authors contributed to the writing of the manuscript. No other authors are involved.

Competing interests
The authors declare no competing interests.

Received: 5 March 2024 Accepted: 7 October 2024 Published online: 15 October 2024

References

1. Bennett CH, Bessette F, Brassard G, Salvail L, Smolin J. Experimental quantum cryptography. J Cryptol. 1992;5(1):3–28. https://doi.org/10.1007/BF00191318.
2. Smolin JA. The early days of experimental quantum cryptography. IBM J Res Dev. 2004;48(1):47–52. https://doi.org/10.1147/rd.481.0047.
3. Brassard G. Brief History of Quantum Cryptography: a Personal Perspective. 2006. https://doi.org/10.48550/ARXIV.QUANT-PH/0604072.
4. Jacobs BC, Franson JD. Quantum cryptography in free space. Opt Lett. 1996;21(22):1854. https://doi.org/10.1364/OL.21.001854.
5. Hughes RJ, Buttler WT, Kwiat PG, Lamoreuax SK, Morgan GL, Nordholt JE, Peterson CG. Quantum cryptography for secure satellite communications. In: 2000 IEEE aerospace conference. Proceedings (cat. No.00TH8484). vol. 1. Big Sky: IEEE; 2000. p. 191–200. https://doi.org/10.1109/AERO.2000.879387. http://ieeexplore.ieee.org/document/879387/.
6. Buttler WT, Hughes RJ, Lamoreaux SK, Morgan GL, Nordholt JE, Peterson CG. Daylight quantum key distribution over 1.6 km. Phys Rev Lett. 2000;84(24):5652–5. https://doi.org/10.1103/PhysRevLett.84.5652.
7. Resch KJ, Lindenthal M, Blauensteiner B, Bohm HR, Fedrizzi A, Kurtsiefer C, Poppe A, Schmitt-Manderbach T, Taraba M, Ursin R, Walther P, Weier H, Weinfurter H, Zeilinger A. Distributing entanglement and single photons through an intra-city, free-space quantum channel. Opt Express. 2005;13(1):202. https://doi.org/10.1364/OPEX.13.000202.
8. Erven C, Couteau C, Laflamme R, Weihs G. Entangled quantum key distribution over two free-space optical links. Opt Express. 2008;16(21):16840. https://doi.org/10.1364/OE.16.016840.
9. Peng C-Z, Yang T, Bao X-H, Zhang J, Jin X-M, Feng F-Y, Yang B, Yang J, Yin J, Zhang Q, Li N, Tian B-L, Pan J-W. Experimental free-space distribution of entangled photon pairs over 13 km: towards satellite-based global quantum communication. Phys Rev Lett. 2005;94:150501. https://doi.org/10.1103/PhysRevLett.94.150501.
10. Jiang L, Dai T, Yu X, Dai Z, Wang C, Tong S. Analysis of scintillation effects along a 7 km urban space laser communication path. Appl Opt. 2020;59(27):8418. https://doi.org/10.1364/AO.397309.
11. Jiang Y, Ma J, Tan L, Yu S, Du W. Measurement of optical intensity fluctuation over an 118 km turbulent path. Opt Express. 2008;16(10):6963. https://doi.org/10.1364/OE.16.006963.
12. Ursin R, Tiefenbacher F, Schmitt-Manderbach T, Weier H, Scheidl T, Lindenthal M, Blauensteiner B, Jennewein T, Perdigues J, Trojek P, Ömer B, Fürst M, Meyenburg M, Rarity J, Sodnik Z, Barbieri C, Weinfurter H, Zeilinger A. Entanglement-based quantum communication over 144 km. Nat Phys. 2007;3(7):481–6. https://doi.org/10.1038/nphys629.
13. Schmitt-Manderbach T, Weier H, Fürst M, Ursin R, Tiefenbacher F, Scheidl T, Perdigues J, Sodnik Z, Kurtsiefer C, Rarity JG, Zeilinger A, Weinfurter H. Experimental demonstration of free-space decoy-state quantum key distribution over 144 km. Phys Rev Lett. 2007;98:010504. https://doi.org/10.1103/PhysRevLett.98.010504.
14. Schmitt-Manderbach T. Long distance free-space quantum key distribution. 2007.
15. Chen Y-A, Zhang Q, Chen T-Y, Cai W-Q, Liao S-K, Zhang J, Chen K, Yin J, Ren J-G, Chen Z, Han S-L, Yu Q, Liang K, Zhou F, Yuan X, Zhao M-S, Wang T-Y, Jiang X, Zhang L, Liu W-Y, Li Y, Shen Q, Cao Y, Lu C-Y, Shu R, Wang J-Y, Li L, Liu N-L, Xu F, Wang X-B, Peng C-Z, Pan J-W. An integrated space-to-ground quantum communication network over 4,600 kilometres. Nature. 2021;589(7841):214–9. https://doi.org/10.1038/s41586-020-03093-8.
16. Liao S-K, Cai W-Q, Liu W-Y, Zhang L, Li Y, Ren J-G, Yin J, Shen Q, Cao Y, Li Z-P, Li F-Z, Chen X-W, Sun L-H, Jia J-J, Wu J-C, Jiang X-J, Wang J-F, Huang Y-M, Wang Q, Zhou Y-L, Deng L, Xi T, Ma L, Hu T, Zhang Q, Chen Y-A, Liu N-L, Wang X-B, Zhu Z-C, Lu C-Y, Shu R, Peng C-Z, Wang J-Y, Pan J-W. Satellite-to-ground quantum key distribution. Nature. 2017;549(7670):43–7. https://doi.org/10.1038/nature23655.
17. Dai H, Shen Q, Wang C-Z, Li S-L, Liu W-Y, Cai W-Q, Liao S-K, Ren J-G, Yin J, Chen Y-A, Zhang Q, Xu F, Peng C-Z, Pan J-W. Towards satellite-based quantum-secure time transfer. Nat Phys. 2020;16(8):848–52. https://doi.org/10.1038/s41567-020-0892-y.
18. Yin J, Li Y-H, Liao S-K, Yang M, Cao Y, Zhang L, Ren J-G, Cai W-Q, Liu W-Y, Li S-L, Shu R, Huang Y-M, Deng L, Li L, Zhang Q, Liu N-L, Chen Y-A, Lu C-Y, Wang X-B, Xu F, Wang J-Y, Peng C-Z, Ekert AK, Pan J-W. Entanglement-based secure quantum cryptography over 1,120 kilometres. Nature. 2020;582(7813):501–5. https://doi.org/10.1038/s41586-020-2401-y.

19. Ghalaii M, Pirandola S. Quantum communications in a moderate-to-strong turbulent space. Commun Phys. 2022;5(1):38. https://doi.org/10.1038/s42005-022-00814-5.
20. Bourgoin J-P, Meyer-Scott E, Higgins BL, Helou B, Erven C, Hübel H, Kumar B, Hudson D, D'Souza I, Girard R, Laflamme R, Jennewein T. Corrigendum: a comprehensive design and performance analysis of low Earth orbit satellite quantum communication (2013 New J Phys 15 023006). New J Phys. 2014;16(6):069502. https://doi.org/10.1088/1367-2630/16/6/069502.
21. Aspelmeyer M, Jennewein T, Pfennigbauer M, Leeb WR, Zeilinger A. Long-distance quantum communication with entangled photons using satellites. IEEE J Sel Top Quantum Electron. 2003;9(6):1541–51. https://doi.org/10.1109/JSTQE.2003.820918.
22. Surendran A, Parihar PS, Banyal RK, Kalyaan A. Development of a lunar scintillometer as part of the national large. Opt Telesc Site Surv. 2018. https://doi.org/10.48550/ARXIV.1802.00372.
23. Chen Z, Tian Y, Lü D. Turbulence parameters in the troposphere—lower stratosphere observed by Beijing MST radar. Remote Sens. 2022;14(4):947. https://doi.org/10.3390/rs14040947.
24. Toyoshima M, Jono T, Nakagawa K, Yamamoto A. Optimum divergence angle of a Gaussian beam wave in the presence of random jitter in free-space laser communication systems. J Opt Soc Am A. 2002;19(3):567. https://doi.org/10.1364/JOSAA.19.000567.
25. Kiasaleh K. On the probability density function of signal intensity in free-space optical communications systems impaired by pointing jitter and turbulence. Opt Eng. 1994;33:3748–57.
26. Hemmati H. Near-Earth laser communications. 2004. http://www.taylorandfrancis.com.
27. Chan VWS. Optical space communications. IEEE J Sel Top Quantum Electron. 2000;6(6):959–75. https://doi.org/10.1109/2944.902144.
28. Klein BJ, Degnan JJ. Optical antenna gain. 1: transmitting antennas. Appl Opt. 1974;13(9):2134–41. https://doi.org/10.1364/AO.13.002134.
29. Bedington R, Arrazola JM, Ling A. Progress in satellite quantum key distribution. npj Quantum Inf. 2017;3(1):30. https://doi.org/10.1038/s41534-017-0031-5.
30. Free space path loss calculator. https://www.electronics-notes.com/articles/antennas-propagation/propagation-overview/free-space-path-loss.php.
31. Siraj Anwar M, Bhardwaj MGRN. India physical environment. 2006. https://ncert.nic.in/textbook.php.
32. Thomas ME. Optical propagation in linear media: atmospheric gases and particles, solid-state components, and water. 2006.
33. Spectral science. http://modtran.spectral.com/.
34. The Bridge Between Data and Science. https://giovanni.gsfc.nasa.gov/giovanni/.
35. Andrews LC. HV (hufnagel–valley) C2 n profile model. In: Field guide to atmospheric optics. 2nd ed. Bellingham: SPIE; 2019. https://doi.org/10.1117/3.2318080.ch87. https://www.spiedigitallibrary.org/eBooks/FG/Field-Guide-to-Atmospheric-Optics-Second-Edition/HV-HufnagelValley-C2-n-Profile-Model/HV-HufnagelValley-C2-n-Profile-Model/10.1117/3.2318080.ch87.
36. Tofsted D, O'Brien S, Vaucher G. An atmospheric turbulence profile model for use in army wargaming applications I. 2006. p. 61.
37. Roddier F. Adaptive optics in astronomy. 1999.
38. Andrews LC, Phillips RL, Yu PT. Optical scintillations and fade statistics for a satellite-communication system. Appl Opt. 1995;34(33):7742–51. https://doi.org/10.1364/AO.34.007742.
39. Andrews LC, Phillips RL, Young CY. Laser beam scintillation with applications. 2001. https://doi.org/10.1117/3.412858.
40. Rarity JG, Tapster PR. Knight P. Corrigendum: ground to satellite secure key exchange using quantum cryptography. New J Phys. 2002;4:069502. https://doi.org/10.1088/1367-2630/16/6/069502.
41. Degnan JJ, Klein BJ. Optical antenna gain. 2: receiving antennas. Appl Opt. 1974;13(10):2397–401. https://doi.org/10.1364/AO.13.002397.
42. Marshall WK. Transmitter pointing loss calculation for free-space optical communications link analyses. Appl Opt. 1987;26(11):2055–12057. https://doi.org/10.1364/AO.26.2055_1.
43. Suzuki Y, Nakagawa K, Jono T, Yamamoto A. Current status of oicets laser-communication-terminal development: development of laser diodes and sensors for oicets program. In: Photonics West. 1997. https://api.semanticscholar.org/CorpusID:110790717.
44. Ali I, Al-Dhahir N, Hershey JE. Doppler characterization for Leo satellites. IEEE Trans Commun. 1998;46(3):309–13. https://doi.org/10.1109/26.662636.
45. Grynberg G, Aspect A, Fabre C, Cohen-Tannoudji C. Introduction to quantum optics: from the semi-classical approach to quantized light. Cambridge: Cambridge University Press; 2010. https://books.google.co.in/books?id=l-l0L8YInA0C.
46. Xavier GB, Walenta N, Faria GV, Temporão GP, Gisin N, Zbinden H, Weid JP. Experimental polarization encoded quantum key distribution over optical fibres with real-time continuous birefringence compensation. New J Phys. 2009;11(4):045015. https://doi.org/10.1088/1367-2630/11/4/045015.
47. Li D-D, Gao S, Li G-C, Xue L, Wang L-W, Lu C-B, Xiang Y, Zhao Z-Y, Yan L-C, Chen Z-Y, Yu G, Liu J-H. Field implementation of long-distance quantum key distribution over aerial fiber with fast polarization feedback. Opt Express. 2018;26(18):22793–800. https://doi.org/10.1364/OE.26.022793.
48. Chatterjee S, Goswami K, Chatterjee R, Sinha U. Polarization bases compensation towards advantages in satellite-based qkd without active feedback. Commun Phys. 2023;6(1):116. https://doi.org/10.1038/s42005-023-01235-8.
49. Lo H-K, Ma X, Chen K. Decoy state quantum key distribution. Phys Rev Lett. 2005;94:230504. https://doi.org/10.1103/PhysRevLett.94.230504.
50. Ma X, Qi B, Zhao Y, Lo H-K. Practical decoy state for quantum key distribution. Phys Rev A. 2005;72(1). https://doi.org/10.1103/physreva.72.012326.
51. Lütkenhaus N. Security against individual attacks for realistic quantum key distribution. Phys Rev A. 2000;61:052304. https://doi.org/10.1103/PhysRevA.61.052304.
52. Ma X, Fung C-HF, Lo H-K. Quantum key distribution with entangled photon sources. Phys Rev A. 2007;76:012307. https://doi.org/10.1103/PhysRevA.76.012307.

53. Elterman L: UV, Visible, and IR Attenuation for Altitudes to 50 Km, 1968. 1968
54. Jennewein T, Simon C, Fougeres A, Babin F, Asadi FK, Kuntz KB, Maisonneuve M, Moffat B, Mohammadi K, Panneton D. QEYSSat 2.0 – white paper on satellite-based quantum communication missions in Canada. 2023.
55. Basak S, Azeemuddin S, Nayak J. Analysis of beam wander and pointing error on laser beam propagation through atmosphere. In: 2018 Asia communications and photonics conference (ACP). 2018. p. 1–3. https://doi.org/10.1109/ACP.2018.8596267.

Publisher's Note